APS physics

CHORUS

This is the accepted manuscript made available via CHORUS. The article has been published as:

Electron spin coherence of silicon vacancies in proton-irradiated 4H-SiC

J. S. Embley, J. S. Colton, K. G. Miller, M. A. Morris, M. Meehan, S. L. Crossen, B. D. Weaver, E. R. Glaser, and S. G. Carter

Phys. Rev. B **95**, 045206 — Published 17 January 2017

DOI: 10.1103/PhysRevB.95.045206

Electron Spin Coherence of Silicon Vacancies in Proton-Irradiated 4H-SiC

J. S. Embley[1], J. S. Colton[1], K. G. Miller[1], M. A. Morris[1], M. Meehan[1], S. L. Crossen[1], B. D. Weaver[2], E. R. Glaser[2], and S. G. Carter[2]

[1]*Department of Physics and Astronomy, Brigham Young University, Provo UT 84602*

[2]*Naval Research Laboratory, Washington DC 20375*

We report T_2 spin coherence times for electronic states localized in Si vacancies in 4H-SiC. Our spin coherence study included two SiC samples that were irradiated with 2 MeV protons at different fluences (10^{13} and 10^{14} cm^{-2}) in order to create samples with unique defect concentrations. Using optically detected magnetic resonance and spin echo, the coherence times for each sample were measured across a range of temperatures from 8 K to 295 K. All echo experiments were done at a magnetic field strength of 0.371 T and a microwave frequency of 10.49 GHz. The longest coherence times were obtained at 8 K, being 270 ± 61 μs for the 10^{13} cm^{-2} proton-irradiated sample and 104 ± 17 μs for the 10^{14} cm^{-2} sample. The coherence times for both samples displayed unusual temperature dependences; in particular, they decreased with temperature until 60 K, then increased until 160 K, then decreased again. This increase between 60 and 160 K is tentatively attributed to a motional Jahn-Teller effect. The consistently longer lifetimes for the 10^{13} cm^{-2} sample suggest that a significant source of the spin dephasing can be attributed to dipole-dipole interactions between Si vacancies or with other defects produced by the proton irradiation. The lack of a simple exponential decay for our 10^{14} cm^{-2} sample indicates an inhomogeneous distribution of defect spins.

PACS numbers: 61.72.jn, 71.55.-i, 76.30.Mi

I. INTRODUCTION

Electronic states localized in the defects of solids have shown great potential for important applications such as single photon emission [1, 2], sensing [3], and quantum computing [4]. The nitrogen-vacancy defect center in diamond (N-V center) has been of particular interest in this regard. Applications such as quantum computing require quantum states that will remain coherent over a sufficiently long period of time [5]. Electrons spins in N-V centers can be controlled and manipulated, and through the use of dynamical decoupling pulse sequences have yielded coherence times of up to 3 ms at 300 K and 600 ms at 77 K [6]. However, the manufacture of appropriate diamond samples and integration into spintronic devices can be difficult and expensive, and thus there is strong interest in identifying other materials which may possess similar useful characteristics. Silicon carbide (SiC) is one such material which has shown significant promise, with similar properties to diamond but potentially easier fabrication [7].

There are many different polytypes of SiC [8]. Each polytype can have a variety of possible defects, and furthermore each defect type may possess unique spin properties [9-11]. Different defects in SiC can be formed and modified through high-energy particle bombardment [12] and annealing [13]. Using optically detected magnetic resonance (ODMR), defects in SiC can be optically initialized, addressed, and read out [14]. Individual defect spins can be isolated and coherently controlled [15, 16]. The optical emission of silicon vacancies is longer in wavelength than that of the N-V center and has substantially less attenuation in optical fibers [7]. Silicon vacancy (V_{Si}) defects in SiC exhibit photoluminescence (PL) [17], can be individually controlled, and have spin coherence lifetimes on the order of 100 μs [16]. In 4H-SiC, the polytype studied in this paper, there are two inequivalent lattice sites where V_{Si} defects can exist, namely the hexagonal (h) and quasi-cubic (k) sites.

A variety of T_2 coherence time measurements have previously been made in 4H-SiC for electronic states in Si vacancies as well as for V_C-V_{Si} divacancy complexes. Native neutral divacancies' spin coherence times have been studied at a few different temperatures; one paper reported T_2 times of 360 μs at 20 K and 50 μs at 300 K[18], and another paper reported comparable times of 184 μs at 20 K (hk or kh divacancies) and 263 μs at 200 K (hh or kk divacancies) [19]. In a separate report at 20 K for one particular sample containing neutral divacancies formed through electron irradiation, measurements yielded T_2 times of up to 1.2 ms [15]. These types of coherence times are often measured through Hahn spin echo; however, through dynamical decoupling pulse sequences such as Carr-Purcell-Meiboom-Gill (CPMG), coherence times can typically be extended [19] as with the N-V center.

With regards to Si vacancies, an ensemble of V_{Si} defects formed through electron irradiation (2 MeV electrons at fluence of 10^{15} cm^{-2}) were measured to have a coherence time of 81 μs at room temperature [14]. A separate study on a similar sample, with Si vacancies formed through electron irradiation, showed T_2 times at room temperature of 160 μs [16]. Finally, a maximum coherence time on the order of hundreds of milliseconds was achieved at 17 K for Si vacancies using dynamic decoupling pulses [20].

Although some of these works have measured the spin coherence times at two temperatures, none has addressed the temperature dependence of T_2 in a systematic fashion. By contrast, the T_1 and T_2^* lifetimes of vacancy defects in SiC have been measured over a range of temperatures by at least two groups. The T_1 of Si vacancies decreased monotonically with increasing temperature [20], whereas the T_2^* of divacancies had a complicated, non-monotonic dependence [21].

In this paper we report T_2 lifetimes for electrons localized at Si vacancies in 4H-SiC, a polytype which has demonstrated significant potential [19]. Measurements were made on two distinct samples, in which the V_{Si} defects in the two samples were created with different fluences of proton irradiation: 10^{13} cm^{-2} and 10^{14} cm^{-2}. Temperatures from 8 K to 295 K were studied. The highest T_2 time for each sample was found at the lowest temperature (8 K): the 10^{13} cm^{-2} sample with a lifetime of 270 ± 61 μs and the 10^{14} cm^{-2} sample with a lifetime of 104 ± 17 μs. The lifetimes for each sample decrease with temperature until about 60 K, then unexpectedly increase from 60 K until 160 K, after which they decrease again. This unusual trend with temperature is very similar to what was seen in SiC divacancy measurements by Falk et al., their overall T_2^* lifetimes being four orders of magnitude shorter than our T_2 lifetimes but in many respects following a similar temperature trend [21]. This trend is tentatively attributed to dynamic averaging from a motional Jahn-Teller effect as has been seen in the C vacancy [22].

II. EXPERIMENTAL METHODS

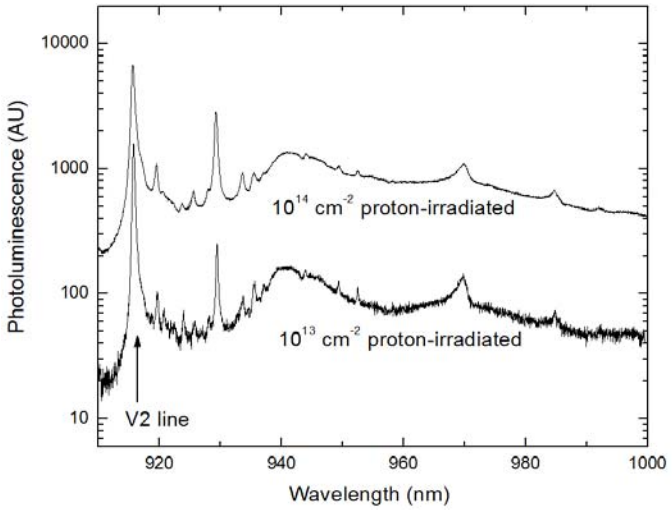

FIG. 1. Photoluminescence of the two main SiC samples with 870 nm excitation. Note the order-of-magnitude increased strength of the spectral peaks for the 10^{14} cm^{-2} sample as compared to the 10^{13} cm^{-2} sample, due to the increased number of vacancy defects. The spectra were both taken at low temperature (5 K and 6 K for the 10^{14} and 10^{13} cm^{-2} samples, respectively).

Each sample consists of high purity semi-insulating SiC (from Cree, Inc.) with the c-axis oriented 8° from the normal to the sample. Si vacancies were generated by irradiating four pieces of the same SiC wafer with 2 MeV protons at fluences of 10^{11}, 10^{12}, 10^{13}, and 10^{14} cm^{-2}. (The vacancy concentration pre-irradiation was negligible.) The 10^{11} cm^{-2} sample was used for spatially-resolved PL to estimate defect concentration, the 10^{12} cm^{-2} sample for depth-dependent PL, and all of the spin-related measurements were made on the 10^{13} and 10^{14} cm^{-2} samples alone. The PL spectra of the 10^{13} and 10^{14} cm^{-2} samples are displayed in Fig. 1; the "V2" line at 916 nm marks the V_{Si} PL emission from the *h* defect site that we used in the spin experiments presented below. We note that the other sharp PL line of comparable intensity observed in this spectral range at 930 nm is not identified at this time.

Defect formation through proton irradiation is of particular interest because the protons have a well-defined stopping distance. It is therefore a step towards controlled patterned placement of these defect centers, as has been done with ion implantation. For example, Falk et al. used 10 keV energy ^{12}C ions at a dose of 10^{13} cm^{-2} to implant divacancy spin ensembles in

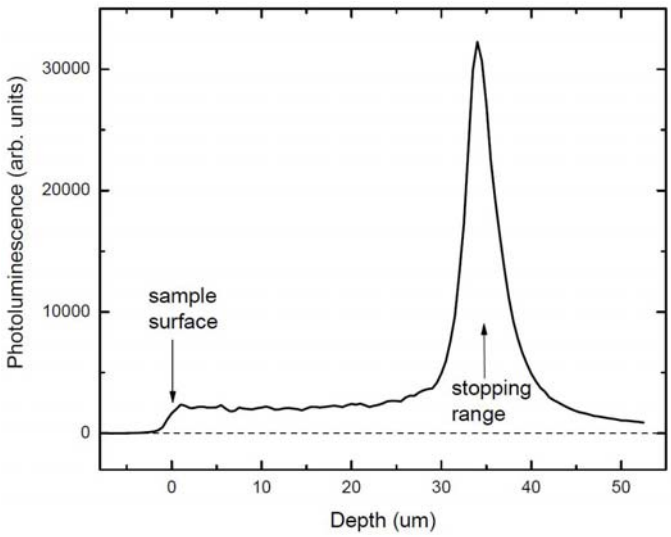

FIG. 2. Depth-dependent photoluminescence of the 10^{12} cm^{-2} sample at the V2 wavelength. The large peak at 34 μm indicates the stopping position of the protons. The spatial resolution was 1 μm.

SiC in a patterned array [18]. From our SRIM (Stopping and Range of Ions in Matter) simulations, the stopping range of the 2 MeV protons is predicted to be 44 μm from the surface. Depth-dependent PL of the 10^{12} cm^{-2} sample shows bright V2 emission centered at a depth of 34 μm, which we interpret as the actual stopping range of the protons; see Fig. 2. This was measured via confocal microscopy on a cleaved edge of the sample, scanning normal to the surface using a 0.7 numerical aperture objective, 780 nm excitation, and at a temperature of 25 K. As can be seen from the figure, the V2 PL—and hence the vacancy defects themselves—extends from the surface to the stopping layer. The vacancies exist in two regimes: a diffuse region ranging from the surface to the stopping layer, and a more concentrated region at the stopping layer itself. The integrated area of the peak vs. that for the diffuse region is larger by about a factor of three.

Photoluminescence from individual vacancies was resolved in the 10^{11} cm^{-2} sample in the diffuse region, also via confocal microscopy, leading to an estimate of 0.3 defects/μm^3 (3×10^{11} cm^{-3}) for that sample. This is only an order of magnitude estimate since we did not have sufficient emission rate to verify that the PL sources were single emitters by e.g. correlated

photon anti-bunching measurements. Assuming the number of defects scales linearly with radiation dose, we estimate the V_{Si} densities of the other three samples to be 3, 30, and 300 μm^{-3}, i.e. 3×10^{12}, 3×10^{13}, and 3×10^{14} cm^{-3}, for their diffuse regions. The densities in the more concentrated regions are estimated to be about 10 times higher than those, based on the depth-dependent PL.

For all of the spin experiments, the samples were placed in a nonmagnetic CryoIndustries cryostat mounted inside a large conventional iron-core electromagnet, with the field perpendicular to the sample face (i.e. 8° from the c-axis). The current for the electromagnet was provided by a Magna-Power Electronics power supply targeting a field strength of 0.371 T and operating in a mode where the output voltage follows an input analog reference voltage. The reference voltage was determined by the built-in PI controller of a Lake Shore Cryotronics gaussmeter whose probe was mounted in the magnet near the sample. Operating the magnet in this configuration provided a field stability of 0.03 mT.

We used an optically-pumped Spectra-Physics cw Ti:sapphire laser tuned to 870 nm to align the spins and induce PL from the sample. The laser was stabilized by a BEOC laser power controller (long-term stability of 0.03%) and then focused onto a NEOS Technologies acousto-optic modulator (AOM), which allowed for optical pulses as short as 20 ns. The laser beam was expanded, re-collimated, then focused onto the sample with a cw-equivalent power of about 350 mW (i.e. the power if the laser had a duty cycle of 100%) and a spot size approximately 100 μm in diameter. The light impacted the sample edge-on, with the vertical polarization direction being along the plane of the surface. Due to the spot size, the depth of the defects as shown in Fig. 2, and the edge-on nature of the alignment, the laser therefore probes defects from all depths and a variable range of defect densities. We employed a 900 nm longpass dichroic

mirror/beam splitter which reflects the laser beam but allows the emitted PL (at about 915 nm) to pass through. Additionally, three 900 nm long pass filters were placed in front of the detector (a Newport 818-SL photodiode) to reduce the amount of scattered laser light mixed in with the PL. Between the beam splitter and filters, scattered laser light at the detector was reduced by a nominal factor of 3×10^{10}.

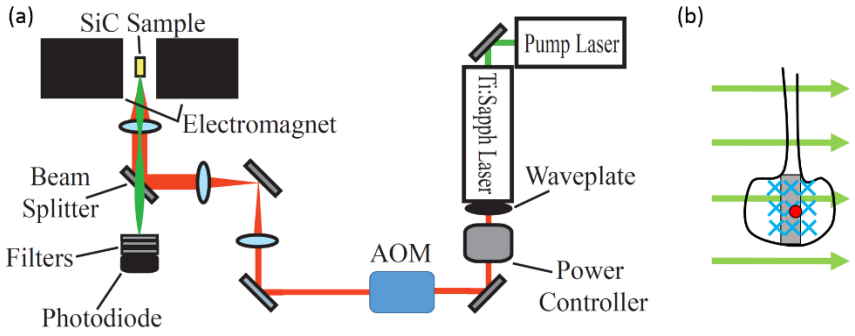

FIG. 3. (a) Schematic of the optical experiment. (b) View of microwave coupling loop (black) and sample (gray) in cryostat, with static magnetic field (green arrows), microwave field (blue arrow tails), and laser beam (red dot, vertically polarized) indicated.

Microwaves at 10.49 GHz, produced by an Agilent Technologies synthesizer at 0 dBm and increased by an Amplifier Research traveling wave tube amplifier to 40 dBm, were used to manipulate the electronic spins. The microwaves were transmitted to the sample via a small coupling loop surrounding the sample, formed by shorting the inner and outer conductors of a coaxial cable. The frequency near 10.49 GHz was selected and a stub tuner was employed to maximize microwave transmission through the loop. The coupling loop was oriented so that the AC magnetic field from the microwaves was orthogonal to the DC field of the electromagnet. See Fig. 3 for a schematic of the optics and the relative orientations of the sample, static magnetic field, microwave field, and laser beam. The microwaves were modulated on and off via a PIN diode switch controlled by an Agilent pulse pattern generator, which also controlled the AOM. When microwave pulse sequences were employed for Rabi and spin echo scans, the sequences were gated on and off at 1 kHz with a Tektronix function generator.

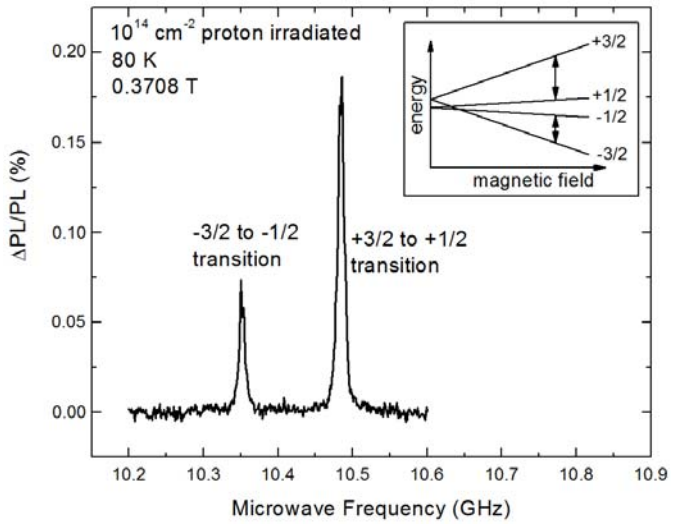

FIG. 4. Representative optically-detected magnetic resonance of the 10^{14} cm^{-2} proton-irradiated sample, at 80 K and 0.3708 T. Two peaks are observed. The signal strength is plotted as a percentage of the total photoluminescence reaching the detector. Inset: energy levels of the spin 3/2 system, with the two observed transitions indicated. The +3/2 ↔ +1/2 transition was used for all echo scans.

The ground state of the V_{Si} defect in 4H-SiC forms a spin 3/2 state [14, 23, 24]. The inset to Fig. 4 depicts the four energy levels schematically. Transitions between the m_s = +3/2 and +1/2, and between the –1/2 and –3/2 states can be observed through ODMR as two peaks separated by 135 MHz; see Fig. 4. We chose to focus on the +3/2 ↔ +1/2 transition, i.e. the higher frequency peak. The ODMR signal at the peak varied from about 0.4% of the PL at low temperatures to 0.1% of the PL at room temperature. The mechanism by which the ODMR occurs involves a spin-dependent non-radiative transition through a metastable state. As a result of this spin-dependent transition, optical pumping with linearly polarized light causes the ±1/2 states to become preferentially populated over the ±3/2 states [16] (or possibly the ±3/2 states may be preferentially populated over the ±1/2 states [25], there is some dispute in the literature). This spin dependent non-radiative process also results in less PL when the system is in this optically pumped set of states [7]. When microwaves induce transitions between the +1/2 and +3/2 states, the populations are equalized causing PL to increase. Thus, the relative amount of PL

detected by the photodiode is reflective of the current state of the spins. To detect such changes we connected the photodiode detector to a Stanford Instruments lock-in amplifier in current mode referenced to the overall microwave pulse sequence on/off gating frequency; the data in Fig. 4 employed a 50% duty cycle.

III. MICROWAVE PULSE SEQUENCES

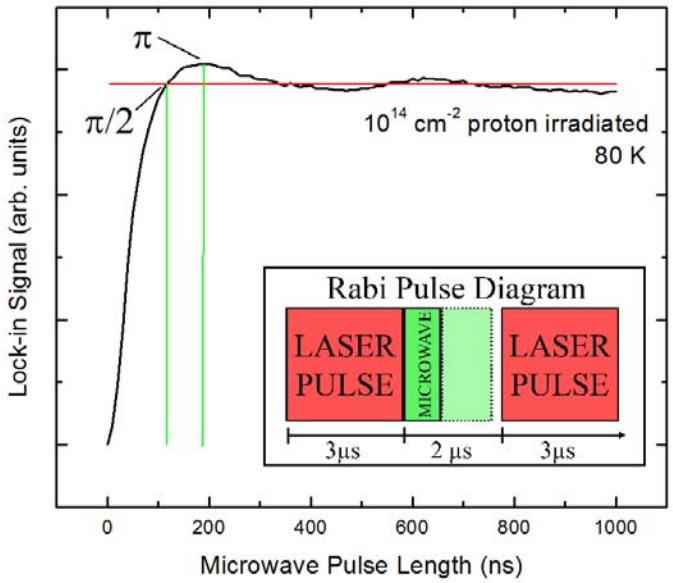

FIG. 5. Representative Rabi oscillation data, for the 10^{14} cm^{-2} sample at 80 K. The vertical lines (green) represent the π and π/2 pulse times deduced from the experiment for those conditions. The horizontal dashed line (red) indicates the zero polarization value. Inset: the laser and microwave pulse sequences for the Rabi experiments.

The two observed transitions can be described by the equations $f_{lower} = -67.3\,MHz + 28.10\frac{GHz}{T} \times B$ and $f_{upper} = +67.3\,\text{MHz} + 28.10\frac{GHz}{T} \times B$, where h is Plank's constant, f is frequency, and B is the magnetic field strength. The slope of the frequency vs. B relates to the electron g-factor; the measured slope gives rise to a g-factor of $g = 2.007$, which is very close to the free electron value of 2.002. These parameters are in good agreement with other measured V2 parameters from the literature [26]. We detect the resonance condition by fixing the static magnetic field and scanning the applied microwaves across a range of frequencies while observing the PL signal.

The spin echo technique requires π/2 and π microwave pulses to manipulate the spin states. The appropriate lengths of these pulses were determined by observing Rabi oscillations. The Rabi oscillation scans were done with a 3 μs laser pulse followed by a variable microwave pulse (between 0 and 2 μs); the two pulses were repeated with a frequency of 174 kHz, i.e. a little slower than 1/(3 μs + 2 μs). The laser pulses serve the dual purpose of stimulating PL,

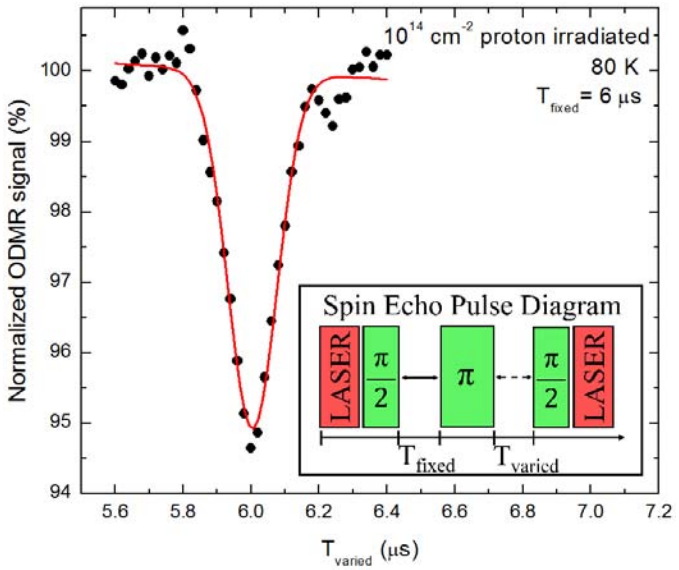

FIG. 6. Representative spin echo data, for the 10^{14} cm^{-2} sample at 80 K and with a T_{fixed} value of 6 μs. The data is normalized so that the y-axis is the ODMR signal divided by the ODMR baseline. The red line represents a Gaussian fit of the data with a linear baseline. The echo strength is defined to be how far the echo changes from 100% towards zero. Inset: the laser and microwave pulse sequences for the spin echo experiments.

which allows the current state of the spins to be read out, and re-initializing the spins for the next period. The variable length microwave pulse causes the spins to flip between the two spin states, resulting in an oscillating PL response. We defined the π pulse length as the time where the PL reaches its first maximum, and the π/2 pulse as the time when the PL reaches its first zero polarization value; see Fig. 5 for a representative case at 80 K where the π/2 and π pulse lengths were 117 and 189 ns, respectively. The π/2 and π pulse lengths were established for each temperature independently in a similar fashion. The strong damping indicates a large amount of inhomogeneous dephasing, with T_2^* times on the order of a few hundred nanoseconds.

As shown in the insert to Fig. 6, the pulse sequence for the spin echo experiments was as follows: a 3 μs pulse from the laser, a π/2 microwave pulse to rotate the spins 90° into a superposition of the two states, a time delay (T_{fixed}) during which the spins precess and dephase due to inhomogeneity, a π microwave pulse to rotate the states another 180°, a second time delay (T_{varied}) to allow the spins to rephase, and finally a second π/2 microwave pulse to rotate the spins back to their initial state for read-out. For each echo scan, we set a value for T_{fixed} then took data

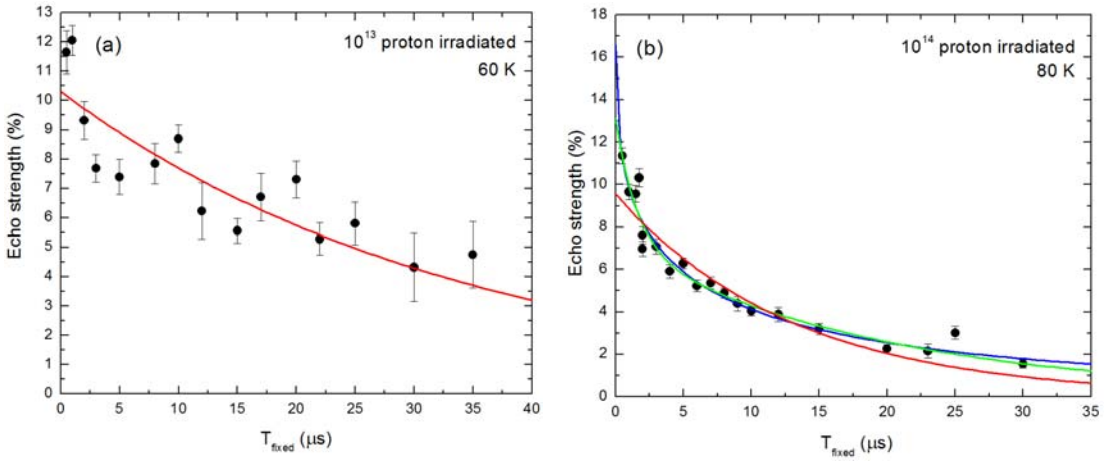

FIG. 7. Representative echo decays for both samples. (a) The 10^{13} cm^{-2} sample at 60 K. The red line is an exponential decay fit as per Eq. 1. (Noise prohibited data collection in for T_{fixed} values longer than 35 μs.) (b) The 10^{14} cm^{-2} sample at 80 K. The red line is an exponential decay fit (Eq. 1); the green line is a biexponential decay fit (Eq. 2); the blue line is a stretched exponential fit (Eq. 3), which overlaps the biexponential fit for most of the decay.

as a function of T_{varied} values. The frequency for the overall pulse sequence was chosen based on the total time required for the laser and microwave pulses and the T_{fixed} and T_{varied} delays, ranging from 165 kHz down to 6 kHz. A representative spin echo scan is plotted in Fig. 6; the minimum corresponds to the echo and is obtained when $T_{varied} = T_{fixed}$. The spin echo is a negative effect because the ODMR signal *increases* when coherence is *lost*; conversely, if phase coherence is retained the electrons will end up in their initial state at the end of the pulse sequence which reduces the signal. For perfect pulse rotations and rephasing, the echo should bring the ODMR signal to zero, but T_2^* limits the rotation fidelity here, as evidenced by the heavily damped Rabi oscillations.

The echoes were well fit to negative Gaussian peaks with linear baselines, and the strength of each echo was characterized as how far the signal dipped from the baseline (plotted as 100%) toward zero. Note that a 5% echo strength, as is for example the case for Fig. 6, represents a 5% change in the ODMR signal, meaning 5% of the "ΔPL/PL" signals discussed above and plotted in Fig. 4 (which were 0.1-0.4%).

IV. RESULTS AND DISCUSSION

For a given temperature, the echo signal decreases in strength as T_{fixed} is increased; this indicates that spin coherence is being lost as a function of time. Representative decays are displayed for both samples in Fig. 7. In the simplest case, the echo strength (y) will decay as

$$y = Ae^{-2T_{fixed}/\tau}, \quad (1)$$

where the fitting parameter τ represents the T_2 spin lifetime. The factor of 2 arises because the total time scale is set by the sum of T_{fixed} and T_{varied}.

Our data for the 10^{14} cm^{-2} sample in many cases cannot be well fit by the simple exponential decay of Eq. (1). We found that, instead, the data can much better be fit either as the sum of two exponential decays,

$$y = A_1 e^{-2T_{fixed}/\tau_{short}} + A_2 e^{-2T_{fixed}/\tau_{long}}, \quad (2)$$

where the parameters τ_{short} and τ_{long} represent decay times of two different populations of defect spins; or as a stretched exponential,

$$y = Ae^{-(2T_{fixed}/\tau)^{\beta}}, \quad (3)$$

where τ represents a characteristic spin coherence time and β characterizes the width of a continuous distribution of times (the distribution going to a delta function in the limit that β approaches 1). There is no a priori reason to favor one functional form over the other and therefore we have fit our data for the 10^{14} cm^{-2} sample to both Eqs. (2) and (3). Figure 7(b) demonstrates the fits for the biexponential and stretched exponential decays (green and blue curves, respectively), along with a single exponential decay (red). Much better fits are obtained using Eqs. (2) and (3). Equation (2) would imply a bimodal distribution of lifetimes, which is plausible given the distribution of V_{Si} defects as shown in Fig. 2, i.e. some vacancies being present in a highly concentrated region and some being present in a more diffuse layer. However,

the values of A_2 (long time component) obtained from the fits are always larger than the values of A_1 (short time component). This is reversed from what one would expect if the two components of the biexponential fit were to directly correspond to the two types of defect distributions seen in Fig. 2, because one would expect the concentrated region with higher integrated PL to have shorter lifetimes than the diffuse region with lower integrated PL. Therefore in the Eq. 2 fit results, the two terms of the biexponential fit are unlikely to directly correspond to the two types of defect distributions.

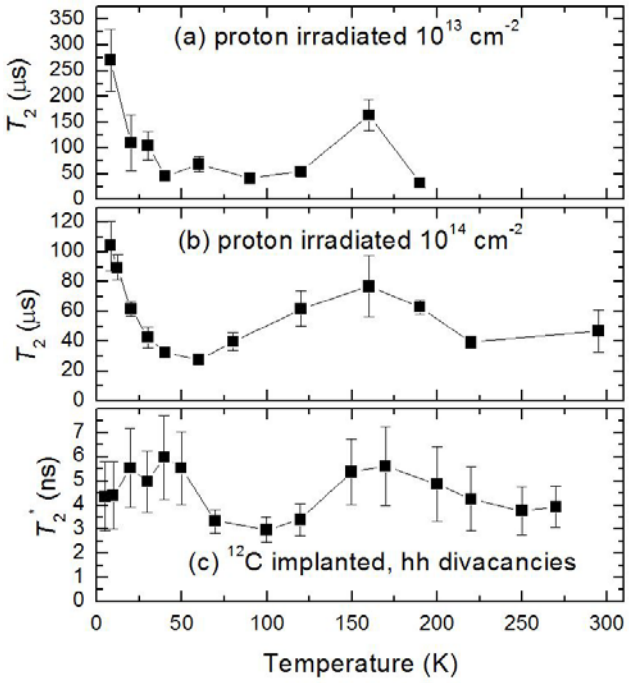

FIG. 8. Temperature dependence of spin lifetimes in SiC. The black connecting lines serve as guides to the eye. (a) T_2 coherence times of 10^{13} cm^{-2} 4H-SiC sample. (Noise prohibited data collection for temperatures higher than 190 K.) (b) T_2 coherence times of 10^{14} cm^{-2} 4H-SiC sample (biexponential τ_{long} values). (c) T_2* times of SiC hh divacancies. Figure 7(c) adapted with permission from Ref. [21]. Copyrighted by the American Physical Society.

Equation (3), in contrast, would imply a continuous distribution of lifetimes, where the parameter β is a measure of the distribution width; when $\beta > 1$ this is a compressed (rather than stretched) exponential function and has been used by others to phenomenologically fit spin echo decay in SiC (with $\beta = 2$) [15]. From our fits of these samples we find $\beta < 1$, i.e. the more normal stretched case; the typical values of β from our fits would correspond to lifetime distributions

having FWHM values ranging from 2.5-14 τ and mean T_2 coherence times of 1.3-3.3 τ. Either way, the lack of a single exponential decay time likely indicates inhomogeneity, which is consistent with both the rapid dephasing of the Rabi oscillations (as shown in Fig. 5) and the distributions of defect densities from the vacancy depth profile.

For the 10^{13} cm^{-2} sample results, due to the increased amount of noise (a result of less PL and longer decay times, which require smaller duty cycles) we could not definitively conclude that a simple single exponential decay was insufficient to fit the data; thus we present in Table I and Fig. 8(a) only a single decay time in the results for this sample. For completeness, in Table II we include the fitting parameters obtained from both Eq. (2) and Eq. (3), although for simplicity Fig. 8(b) just includes the Eq. (2) value of τ_{long} for the 10^{14} cm^{-2} sample. As can be readily seen, the spin coherence times for the 10^{13} cm^{-2} sample for most temperatures are a factor of 1.5-2.5 larger than the coherence times of the 10^{14} cm^{-2} sample (comparing vs. the τ_{long} values).

The longest coherence times are found at the lowest temperatures and in general decrease as the temperature is increased, but surprisingly the lifetimes increase from about 60 K until 160 K, before decreasing again. When the overall trend is viewed, the coherence times in both samples appear to be enhanced in the region from 60-160 K. This behavior is remarkable, as the dominant spin dephasing mechanisms usually result in a continuous decrease of spin lifetime with temperature. For example, in both experimental and theoretical studies of the T_1 spin lifetime of the V_{Si} defect in SiC, T_1 vs. temperature changes monotonically from 5 K to 300 K as a result of phonon-assisted spin relaxation mechanisms [20].

As a possible explanation for the increase in spin coherence time in the 60-160 K region, we suggest the dynamic Jahn Teller effect. A similar non-monotonic temperature behavior has been seen in the positively charged carbon vacancy, V_C, of 4H-SiC [22]. In that work, the authors

found that the low temperature vacancy structure was characterized by the pairing of orbitals of the four neighboring Si atoms due to Jahn-Teller distortion (Si1-Si2 and Si3-Si4). Dynamic reorientation at higher temperatures was seen through the effects of EPR and pulsed EPR on the V_C hyperfine lines. The authors measured T_2 through the spin echo decay as well as through the width of resonance lines. They found two regimes: below 40 K they observed lifetime broadening where T_2 decreased with temperature. Above 40 K they found motional narrowing where T_2 increased with temperature. The motional narrowing was attributed to a thermally activated reorientation of the vacancy, with a 14 meV activation energy. In other words, rapid thermally-activated reorientations (bond switching) change the character of the vacancy, and cause the spin lifetime to increase rather than decrease with temperature.

A similar temperature dependence to our T_2 data was seen for T_2^* by Falk et al. [21] in V_C-V_{Si} divacancies in 6H-SiC. We have plotted their data for hh divacancies in Fig. 8(c). Aside from the initial rise in lifetime with temperature, their data displays a very similar temperature dependence to our own. They also observed a similar effect for kk divacancies which for simplicity we have not plotted. Their T_2^* times are four orders of magnitude smaller than our T_2 times, which makes the similarity in temperature dependence all the more striking. They also attribute some of the non-monotonic behavior to the motional narrowing/dynamic Jahn-Teller effect. The similarities between SiC vacancy-related spin lifetimes seen in the V_{Si} (this work), the V_C [22], and the V_{Si}-V_C divacancy [21], despite differences in samples and defect centers, seem to indicate that the motional Jahn-Teller effect may play a fundamental role in affecting spin dephasing in such materials.

Lastly, we note that the times for the 10^{13} cm^{-2} sample were consistently longer than for the 10^{14} cm^{-2} sample. This suggests that a significant source of the spin dephasing can be

attributed to dipole-dipole interactions with proton-irradiation induced defects; the interactions could be between two nearby V_{Si} centers or between a V_{Si} center and other defects. Other studies that have found dipole-dipole interactions to be the dominant factor in dephasing in V_{Si} centers [16, 26]. For example, Widmann et al. [16] estimated that concentrations of 10^{16} cm^{-3} spins should give rise to ~100 μs spin decoherence times, with time being inversely proportional with spin concentration. This is fairly consistent with our results, although an exact inverse scaling, ignoring other mechanisms, would predict times of ~3000 μs in the concentrated region of the 10^{13} cm^{-2} irradiated sample (V_{Si} concentration of $\sim 3 \times 10^{14}$ cm^{-3} in that region) and ~300 μs in the concentrated region of the 10^{14} cm^{-2} irradiated sample (V_{Si} concentration of $\sim 3 \times 10^{15}$ cm^{-3} in that region). Of course other radiation-induced defects will also be present, and our measured lifetimes being lower than those predictions from the scaling may indicate that important dipole-dipole interactions may also be going on between the V_{Si} centers and other radiation-induced defects (possibly carbon vacancies or divacancies), as well as between the V_{Si} centers themselves.

V. CONCLUSION

We have measured T_2 spin coherence times for electronic states of the V_{Si} defect center in proton-irradiated 4H-SiC. The coherence times were as long as 270 μs for the 10^{13} cm^{-2} proton-irradiated sample at 8 K. In addition, the times for the 10^{13} cm^{-2} sample were consistently longer than for the 10^{14} cm^{-2} sample, which indicates dipole-dipole interactions with radiation-induced defects are a source of dephasing. The coherence times followed a non-monotonic dependence on temperature, with the unexpected rise in lifetime with temperature in the 60-160 K range possibly explained by motional narrowing arising from a dynamic Jahn-Teller effect similar to

what has been observed in the V_C [22], and the V_{Si}-V_C divacancy [21]. Lastly, the lack of a simple exponential decay for the 10^{14} cm^{-2} proton-irradiated sample points to an inhomogeneous population of defect spins, possibly a bimodal distribution or one with a more complex distribution of lifetimes. This may be due to our sampling of regions of varying defect density inside the optical focus.

ACKNOWLEDGMENTS

J. S. Embley, K. G. Miller, and M. A. Morris were partially or fully supported through the NSF REU program, grant number PHY-1461219. M. A. Morris was a visiting student from Brandeis University. S. G. Carter and E. R. Glaser acknowledge support from the U.S. Office of Naval Research and the OSD ARAP Quantum Sciences and Engineering Program. The authors also thank Michel Bockstedte for a helpful theoretical discussion.

TABLE I. Fitted spin lifetimes for the 10^{13} cm^{-2} proton irradiated sample.

Temperature (K)	Single Exponential Fit τ (μs)
8	270 ± 61
20	110 ± 55
30	105 ± 28
40	45 ± 10
60	69 ± 14
90	41 ± 8
120	55 ± 11
160	164 ± 30
190	32 ± 9

TABLE II. Fitted spin lifetimes for the 10^{14} cm^{-2} proton irradiated sample.

Temperature (K)	Biexponential Fit		Stretched Exponential Fit	
	τ_{short} (μs)	τ_{long} (μs)	β	τ (μs)
8	8 ± 5	104 ± 17	0.6 ± 0.1	79 ± 6
12	9 ± 5	90 ± 8	0.7 ± 0.1	70 ± 3
20	1.1 ± 0.4	62 ± 5	0.4 ± 0.1	34 ± 11
30	6 ± 4	43 ± 7	0.7 ± 0.1	28 ± 3
40	1.3 ± 1.0	32 ± 2	0.6 ± 0.1	21 ± 3
60	1.8 ± 0.6	28 ± 3	0.4 ± 0.1	8 ± 3
80	3 ± 1	40 ± 6	0.4 ± 0.1	9 ± 5
120	7 ± 3	62 ± 12	0.6 ± 0.1	34 ± 3
160	12 ± 9	77 ± 21	0.7 ± 0.1	51 ± 4
190	2.3 ± 0.6	63 ± 5	0.5 ± 0.1	32 ± 6
220	1.7 ± 1.4	40 ± 4	0.7 ± 0.1	30 ± 3
295	5 ± 3	47 ± 14	0.5 ± 0.1	22 ± 5

References

[1] S. Castelletto, B.C. Johnson, V. Ivády, N. Stavrias, T. Umeda, A. Gali, T. Ohshima, Nat. Mater., **13**, 151 (2014).

[2] A. Lohrmann, N. Iwamoto, Z. Bodrog, S. Castelletto, T. Ohshima, T.J. Karle, A. Gali, S. Prawer, J.C. McCallum, B.C. Johnson, Nat. Commun., **6**, (2015).

[3] H. Kraus, V.A. Soltamov, F. Fuchs, D. Simin, A. Sperlich, P.G. Baranov, G.V. Astakhov, V. Dyakonov, Sci. Rep., **4**, 5303 (2014).

[4] R.J. Epstein, F.M. Mendoza, Y.K. Kato, D.D. Awschalom, Nat. Phys., **1**, 94 (2005).

[5] C.H. Bennett, D.P. DiVincenzo, Nature, **404**, 247 (2000).

[6] N. Bar-Gill, L.M. Pham, A. Jarmola, D. Budker, R.L. Walsworth, Nat. Commun., **4**, 1743 (2013).

[7] P.G. Baranov, A.P. Bundakova, A.A. Soltamova, S.B. Orlinskii, I.V. Borovykh, R. Zondervan, R. Verberk, J. Schmidt, Phys. Rev. B, **83**, 125203 (2011).

[8] F. Bechstedt, P. Käckell, A. Zywietz, K. Karch, B. Adolph, K. Tenelsen, J. Furthmüller, phys. stat. sol. (b), **202**, 35 (1997).

[9] D. Riedel, F. Fuchs, H. Kraus, S. Väth, A. Sperlich, V. Dyakonov, A.A. Soltamova, P.G. Baranov, V.A. Ilyin, G.V. Astakhov, Phys. Rev. Lett., **109**, 226402 (2012).

[10] V.A. Soltamov, A.A. Soltamova, P.G. Baranov, I.I. Proskuryakov, Phys. Rev. Lett., **108**, 226402 (2012).

[11] N.T. Son, P. Carlsson, J. ul Hassan, E. Janzén, T. Umeda, J. Isoya, A. Gali, M. Bockstedte, N. Morishita, T. Ohshima, H. Itoh, Phys. Rev. Lett., **96**, 055501 (2006).

[12] H. Itoh, N. Hayakawa, I. Nashiyama, E. Sakuma, J. Appl. Phys., **66**, 4529 (1989).

[13] W.E. Carlos, N.Y. Garces, E.R. Glaser, M.A. Fanton, Phys. Rev. B, **74**, 235201 (2006).

[14] S.G. Carter, Ö.O. Soykal, P. Dev, S.E. Economou, E.R. Glaser, Phys. Rev. B, **92**, 161202 (2015).

[15] D.J. Christle, A.L. Falk, P. Andrich, P.V. Klimov, J.U. Hassan, Nguyen T. Son, E. Janzén, T. Ohshima, D.D. Awschalom, Nat. Mater., **14**, 160 (2015).

[16] M. Widmann, S.-Y. Lee, T. Rendler, N.T. Son, H. Fedder, S. Paik, L.-P. Yang, N. Zhao, S. Yang, I. Booker, A. Denisenko, M. Jamali, S.A. Momenzadeh, I. Gerhardt, T. Ohshima, A. Gali, E. Janzén, J. Wrachtrup, Nat. Mater., **14**, 164 (2015).

[17] E. Sörman, N.T. Son, W.M. Chen, O. Kordina, C. Hallin, E. Janzén, Phys. Rev. B, **61**, 2613 (2000).

[18] A.L. Falk, B.B. Buckley, G. Calusine, W.F. Koehl, V.V. Dobrovitski, A. Politi, C.A. Zorman, P.X.L. Feng, D.D. Awschalom, Nat. Commun., **4**, 1819 (2013).

[19] W.F. Koehl, B.B. Buckley, F.J. Heremans, G. Calusine, D.D. Awschalom, Nature, **479**, 84 (2011).

[20] D. Simin, H. Kraus, A. Sperlich, T. Ohshima, G.V. Astakhov, V. Dyakonov, arXiv:1602.05775v1, (2016).

[21] A.L. Falk, P.V. Klimov, V. Ivády, K. Szász, D.J. Christle, W.F. Koehl, Á. Gali, D.D. Awschalom, Phys. Rev. Lett., **114**, 247603 (2015).

[22] T. Umeda, J. Isoya, N. Morishita, T. Ohshima, T. Kamiya, A. Gali, P. Deák, N. T. Son, and E. Janzén, Phys. Rev. B, **70**, 235212 (2004).

[23] H. Kraus, V.A. Soltamov, D. Riedel, S. Vath, F. Fuchs, A. Sperlich, P.G. Baranov, V. Dyakonov, G.V. Astakhov, Nat. Phys., **10**, 157 (2014).

[24] N. Mizuochi, S. Yamasaki, H. Takizawa, N. Morishita, T. Ohshima, H. Itoh, J. Isoya, Phys. Rev. B, **66**, 235202 (2002).

[25] Ö.O. Soykal, P. Dev, S.E. Economou, Phys. Rev. B, **93**, 081207 (2016).

[26] V.A. Soltamov, B.V. Yavkin, D.O. Tolmachev, R.A. Babunts, A.G. Badalyan, V.Y. Davydov, E.N. Mokhov, I.I. Proskuryakov, S.B. Orlinskii, P.G. Baranov, Phys. Rev. Lett., **115**, 247602 (2015).